The effects of post-fabrication annealing on the mechanical properties of freestanding nanoporous gold structures

Erkin Seker [a], John T. Gaskins [b], Hilary Bart-Smith [c], Jianzhong Zhu [a], Michael L. Reed [a], Giovanni Zangari [d], Robert Kelly [d], Matthew R. Begley [a,c,d,*]

[a] *Department of Electrical and Computer Engineering, University of Virginia, Charlottesville, VA 22904, USA*
[b] *Department of Civil Engineering, University of Virginia, Charlottesville, VA 22904, USA*
[c] *Department of Mechanical and Aerospace Engineering, University of Virginia, Charlottesville, VA 22904, USA*
[d] *Department of Materials Science and Engineering, University of Virginia, Charlottesville, VA 22904, USA*

Abstract

The elastic modulus, residual stress and porosity of nanoporous gold are reported for freestanding microfabricated beams and blanket films on substrates. After fabrication, the nanoporous samples were annealed at various temperatures (up to 400 °C) to induce changes in porosity and mechanical properties. The porosity of the samples was characterized by digital processing of scanning electron microscopy images; mechanical properties were measured using combinations of freestanding beam deflection, wafer curvature and nanoindentation. The relative density of all sample geometries increased as the annealing temperature was increased. However, the evolution of the average pore size (with annealing) depended on the geometry, and hence on the boundary conditions, of the specimen. Differences in porosity evolution were reflected in the mechanical property measurements: while the elastic modulus and residual stress generally increased with increasing annealing temperature (due to densification), pore coalescence in films on substrates leads to the most dramatic changes.
© 2007 Acta Materialia Inc. Published by Elsevier Ltd. All rights reserved.

Keywords: Porous material; Annealing; Thin films; Self-organization and patterning

1. Introduction

Nanoporous gold (np-Au) is a promising material for numerous applications, e.g. sensors, catalysts and coatings for medical devices, due to its increased surface area, chemical inertness and biological compatibility [1,2]. Nanoporous gold can be obtained from gold alloys via selective dissolution, also commonly referred to as leaching or dealloying. In this process, a less noble constituent of the alloy is removed chemically to produce a porous structure. Previous research has used bulk alloys and thin foils to address the mechanisms of dealloying [3–9], and investigated the effects of halide-containing electrolytes on critical potential and the resulting pore size [10]. Aside from early pioneering work on fracture of np-Au strips cut from bulk AuAg alloys [11], the mechanical properties of nanoporous metals have only recently begun to attract significant attention: examples include nanoindentation of bulk np-Au discs [12,13] and compression tests on microfabricated posts via nanoindentation [14]. Related research focuses on applications of np-Au includes quartz crystal sensors [15], fabrication of np-Au wires [16] and their implementation as chemical sensors [17].

Recently, our group has demonstrated a versatile microfabrication process to generate freestanding np-Au structures using conventional sacrificial micromachining techniques [18]. The "MEMS-type" microstructures created by this process are amenable to mass production and integration with electronics, and should broaden the

---
* Corresponding author. Address: Department of Mechanical and Aerospace Engineering, University of Virginia, Charlottesville, VA 22904, USA. Tel.: +1 434 243 8728.
   E-mail address: begley@virginia.edu (M.R. Begley).

range of application for nanoporous metals. Freestanding structures also offer new possibilities regarding mechanical characterization; interactions between the film and substrate are eliminated, enabling one to independently determine modulus and residual stress. Moreover, freestanding beam structures have fundamentally different stress states due to their geometric constraints, and this results in different modes of mass transport (i.e. morphology change) than those found in films on substrates.

The focus of this work is on establishing quantitative connections between porosity and mechanical properties of freestanding structures, while providing a comparison with the behavior of blanket films. After fabrication (i.e. patterning, release and dealloying), the structures are subjected to annealing treatments at different temperatures. This use of thermal treatments serves two purposes: first, it systematically varies the porosity of the materials and enables a study of the connections between morphology and mechanical properties. Secondly, it provides an initial evaluation of thermal treatment as a pathway to modulate mechanical properties and control device performance.

2. Sample preparation

2.1. Fabrication of freestanding nanoporous structures

Freestanding np-Au beams were produced by dealloying 40 at.% Au–60 at.% Ag alloy beams that were patterned on silicon wafers. Fig. 1 summarizes the main steps of the fabrication process; further details of the process can be found in our recent paper [18]. The critical initial fabrication step is to create a planar foundation composed of patterned aluminum (Al) sacrificial and chrome (Cr) adhesion layers. This greatly reduces the likelihood of beam failure at the clamp–beam interface by eliminating stress concentrations at the clamp edge that are created by steps in the foundation. After the planar foundation has been laid, an 800 nm thick layer of $Au_{0.4}Ag_{0.6}$ layer is deposited through a photoresist lift-off mask. The ends of the beam were then secured by depositing and patterning 50 nm of Cr and 500 nm of Au over the beam pedestals; these "clamps" were reinforced by 3 μm thick electroplated Au (Fig. 1a). Before releasing the beams, the silicon wafer was scribed with a dicing saw to form a matrix of 18 identical dice. Each die consisted of an assortment of beams that varied in width between 5 and 40 μm and in length between 25 and 500 μm. In order to assure processing uniformity for all beams, the wafer was not sawed through until the entire wafer went through the beam-releasing and drying steps.

After dicing the wafer, the sacrificial aluminum layer was completely removed by an overnight etch in an alkaline solution of AZ400K developer. Each die was then rinsed in deionized (DI) water, and immersed in buffered oxide etchant for 15 min to remove the thermal oxide coating. To release the beams, the silicon was etched (anisotropically) using 30% potassium hydroxide solution; this
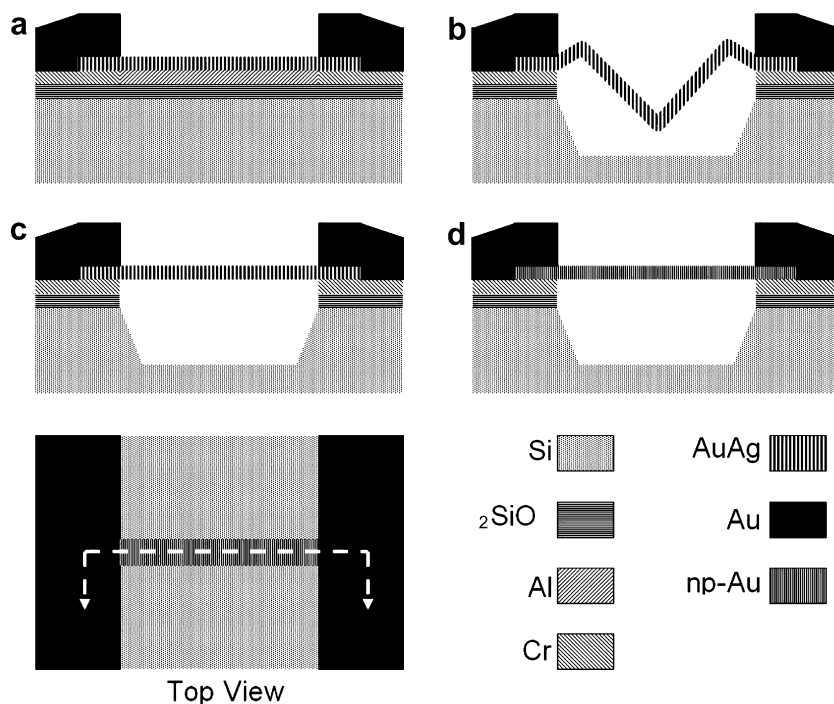

Fig. 1. Fabrication of freestanding $Au_{0.4}Ag_{0.6}$ beams: (a) A patterned layer of AuAg alloy (800 nm) is deposited on a planar foundation of Cr adhesion and Al sacrificial layers (100 nm), and secured with patterned clamps (Cr: ∼50 nm, Au: ∼500 nm); these are reinforced by electroplating thick layers of Au (3 μm). (b) The beam is released by successively etching the Al, SiO₂, and Si; and dried in a critical point dryer. (c) The beams were annealed at 325 °C for 10 min, which induces thermal buckling and mitigates tensile stress during dealloying. (d) The beams were dealloyed in nitric acid, and dried in a critical point dryer.

created 15 μm deep channels running underneath the beams. After the release step, each die was rinsed in DI water and isopropanol (IPA) successively and dried in a critical point dryer (CPD) to complete the fabrication of freestanding AuAg alloy beams (Fig. 1b).

It has been observed by our group and others [18,19] that dealloying produces significant volume shrinkage in bulk AuAg cubes and foils. This shrinkage translates into tensile stress for clamped beams. Consequently, without heat treatment prior to dealloying, the freestanding beams are prone to tensile failure (look ahead to Fig. 7b). Annealing the freestanding AuAg alloy beams before dealloying prevents failure; companion papers describe the effects of annealing prior to dealloying [18,20]. A group of six dice was broken off the wafer and thermally annealed with an AXIC Inc., as-one rapid thermal processor (RTP) at 325 °C for 10 min in nitrogen at atmospheric pressure. This temperature is sufficient to induce thermal plastic buckling, as shown schematically in Fig. 1c. The temperature ramping rate was $20 °C s^{-1}$, and the sample was removed from the RTP after 4 min of cooling when the temperature dropped below 50 °C. The annealed AuAg beams were then dealloyed in 65% nitric acid (HNO_3) at 95 °C for 10 min to produce freestanding np-Au beams, rinsed in DI and IPA, and dried in a CPD. Energy dispersive X-ray spectroscopy (EDS) of the freestanding np-Au beams did not detect any Ag after dealloying.

In the following, two types of cantilevers are discussed: 25 μm long beams that cracked during dealloying were used to study the effects of annealing on freestanding stress-free beams. A second set of cantilevers was created after annealing by cutting intact clamped beams in half along the width using a FEI 200 Ga^+ focused ion beam (FIB) tool. These "FIB-cut" cantilevers were used to measure the elastic modulus of clamped beams.

2.2. Fabrication of blanket films on silicon wafers

To complement the study of freestanding structures, comparable films of np-Au were deposited on identical silicon wafers. When AuAg is dealloyed, blanket films of np-Au peel unless there is an adhesion layer that is resistant to HNO_3. Hence, each wafer was first sputtered with a 15 nm thick Cr then a 15 nm thick Au adhesion layer, followed by a blanket layer of alloy identical to that used for the beam fabrication, i.e. 800 nm of $Au_{0.4}Ag_{0.6}$. (Note that freestanding np-Au structures do not have this adhesion layer, but they are secured at their ends with Cr/Au clamps to prevent peeling.) Following the deposition, samples were dealloyed in HNO_3 at 95 °C for 1 h. EDS of the dealloyed films detected less than 10% Ag by atomic weight in the np-Au film. To account for the effect of the Cr/Au adhesion layer in wafer curvature measurements on np-Au blanket films, identical silicon wafers were coated with a 30 nm thick Cr/Au layer and used as control samples during annealing experiments.

2.3. Post-fabrication annealing experiments

A post-fabrication annealing protocol was used to systematically vary the porosity structure and explore connections between the microstructure and mechanical properties of freestanding np-Au beams and films. Annealing at different temperatures produced repeatable and systematic changes in porosity, modulus and residual stress. Each die, containing np-Au beams and cantilevers, was annealed at 200, 300 and 400 °C for 10 min under the same conditions (purge gas, ramp rate, cooling, etc.) described in Section 2.1. These samples were then subjected to various testing techniques to fully characterize the annealing experiments.

3. Post-annealing characterization methods

3.1. Geometry and porosity characterization

The porosity of the samples was characterized using micrographs obtained with a Zeiss FESEM SUPRA 40 scanning electron microscope (SEM). The SEM images were post-processed with WCIF ImageJ digital imaging software [21]. This required each SEM image to be converted from an original bit depth of 8 (256 shades of gray) to a monochrome binary image. To obtain the monochrome binary image, a threshold shade has to be specified. For consistency, an automatic thresholding algorithm called IsoData (included as a WCIF ImageJ plug-in) was used on all images. To illustrate the effects of the chosen threshold, results are shown in the next section for threshold shades 10% above and below the threshold determined by IsoData (look ahead to Fig. 3). A comprehensive study of thresholding algorithms and their performance can be found elsewhere [22].

Following annealing, beam thickness was measured using SEM imaging of the cross-section of a beam after it was cut with the FIB. A practical FIB cutting method was devised in order to examine easily the beam cross-section; beams were first partially cut in the width direction at an arbitrary location. Then another shallow cut was made approximately 10 μm away from and parallel to the initial cut. The second cut strained the 10 μm rectangular piece and tilted it upwards until it was nearly perpendicular to the top plane of the beam. It was found that a 30 keV beam with 70 pA ion current produced a clean cut without affecting the beam thickness. In order to examine spatial variation in beam thickness, thickness measurements were performed on three distinct FIB-cut beams.

3.2. Mechanical property measurements for freestanding structures

Following the annealing experiments, beams were probed using an MTS nanoindenter equipped with a dynamic contact module (DCM) and a Berkovich diamond tip. Tests were conducted using a method that precisely

identifies the instant of contact by observing changes in a small harmonic load oscillation that is superimposed on top of the ramp loading (during approach) [23]. By identifying the point where harmonic displacement drops precipitously (below the environmental noise), the position of the probe at the instant of contact can be determined to within 1 nm. This precision enables accurate calculations of the load on the sample, even for structures with ultra-low stiffness in the range of $\sim 1 \ N \ m^{-1}$. Three different beams from each of the 100 and 150 μm long sets were tested for each annealing temperature; each beam was indented at its center three times. Hence, the presented data reflect the average of nine tests and their standard deviation. A mixture of 15 and 30 μm wide beams for each length was tested, and it was observed that there was not a significant difference in the stiffness of the two widths.

Because the microstructures of clamped beams and cantilevers respond differently to annealing temperature, "broken" cantilevers could not be used to determine the elastic modulus of annealed beams. Therefore, three annealed beams from 15 and 30 μm wide beams were cut into cantilevers using the FIB tool, and elastic modulus measurements were obtained based upon load–deflection measurements. FIB-cut cantilevers were tested with a slightly different procedure to that used for the beams. Instead of indenting at a single point, three cantilevers per annealing temperature were tested at successive distances (i.e. 22–30 μm in 2 μm steps) from the clamp over the substrate. This procedure generated several experimental stiffness values to calculate an average elastic modulus for each cantilever.

3.3. Mechanical characterization of blanket films

Prior to coating silicon wafers with films of interest, intrinsic surface profiles of wafers were measured with a scanning laser wafer curvature measurement system (Frontier Semiconductor Inc., Model FSM-8800). The wafers were then coated with the Cr/Au adhesion layer and the AuAg film as described in the fabrication section. Wafer curvature measurements were then repeated for the coated wafers, both before and after dealloying. The same annealing schedule was repeated for each wafer as for the beams, with one difference: instead of a fixed annealing time of 10 min, each wafer was first annealed for 2.5 min, and a wafer curvature measurement, film thickness measurement (using a Wyko NT1100 Optical Profiler white light interferometer) and SEM image were taken. Then, each wafer was annealed for a further 7.5 min before again taking the curvature and thickness measurements, and an SEM image. The presence of the Cr/Au adhesion layer affected the radius of curvature, and thus influences the residual stress of the np-Au films during heat treatment. To exclude the effect of the adhesion layer on radius of curvature, identical heat treatment and wafer curvature experiments were performed on wafers coated only with the Cr/Au adhesion layer. Three consecutive

wafer curvature measurements were performed on each wafer after each process step (i.e. deposition, dealloying, annealing), and the data were averaged. The elastic modulus of the blanket films was characterized by conventional nanoindentation techniques, using the MTS DCM module. The tip geometry was calibrated over the range of 0–500 nm, using a fused silica calibration sample; the results indicated that the elastic modulus was independent of penetration depth for depths less than ~100 nm. (Greater depths exhibited increases in modulus due to the presence of the substrate.) The reported values are averages from 10 indents, taken over depths ranging from 20 to 100 nm, with the lower threshold identified as the minimum depth for which the tip calibration yields accurate results on the calibration sample.

4. Results and discussion

4.1. Porosity and geometry analysis

Typical SEM images for the np-Au clamped beams, cantilevers and films for various thermal treatments are compiled in Fig. 2. All images are at the same magnification; as such, the single scale-bar shown in the figure applies to each image. Fig. 3 presents the results from the digital image processing of these images. Percent porosity refers to the area of "dark" portions of the image relative to the total area, as determined by the IsoData algorithm. This algorithm performs pixel-by-pixel processing of an SEM image to determine the number of pixels with intensity above a prescribed cut-off value, and thereby distinguishes between "solid" and "void". This pixel-by-pixel approach presumably eliminates any bias arising from absolute pore size and distribution. Multiple images of an area 2.5×1.9 μm (at $150,000 \times$ magnification) were processed: the deviation in calculated porosity from image to image is much smaller than that introduced by changing the prescribed cut-off value. Hence, we present results with error bars indicating the effect of changing the cut-off value by ±10% from the threshold shade determined automatically by the IsoData algorithm. Both Figs. 2 and 3 demonstrate that the initial porosity (prior to annealing) is similar for all three sample geometries.

The evolution of porosity with annealing is a strong function of geometric boundary conditions, which generate different stress states in each of the three samples (i.e. film, beam, cantilever) and provide different constraints against mass transport and mechanical deformation. After annealing the samples at 200 °C for 10 min, a noticeable change in porosity is evident for the blanket film geometry, while there is minimal change for the freestanding structures. Films constrained on substrates experience biaxial stress that promotes pore growth. Conversely, cantilevers obviously have greatest freedom for geometric change since they are essentially stress-free, i.e. there is no tensile stress to drive pore expansion. Consequently, the pores shrink as the cantilevers become thinner and shorter. SEM images
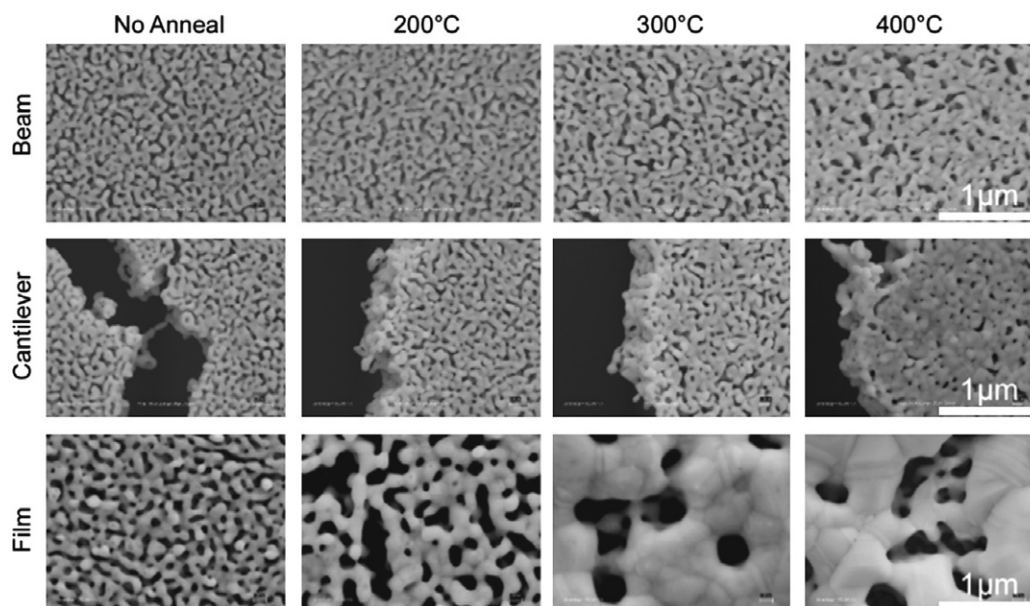
Fig. 2. SEM images for np-Au beams, cantilevers, and films. The porosity of all three structures decreases as the heat treatment temperature increases. Beams develop micro-cracks in response to accumulation of tensile stress. Cantilevers contract as pores vanish. Films display the evolution of large clusters of Au enclosing pores that vary in size with increasing temperature.
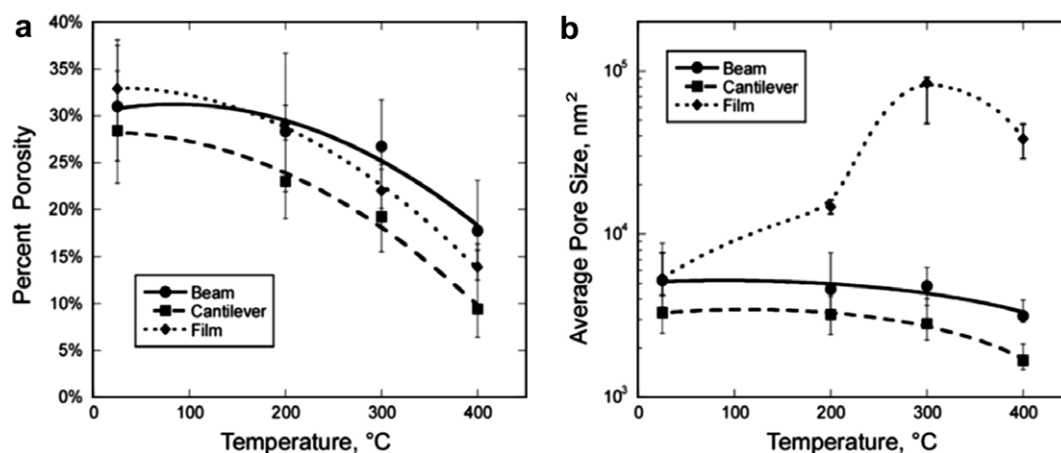

Fig. 3. Percent pore coverage (a), and average pore size (b) for np-Au beams, cantilevers, and films for 10-min heat-treatments at 200, 300, and 400 °C. Curves are added simply as visual guides.

reveal that the ends of the cantilevers[1] retract from each other (as compared to their proximity prior to annealing).

In contrast, the stress for clamped beams is predominantly uniaxial (along the major axis of the beam), and there is relatively little constraint against contractions in both the width and thickness directions. As a result, beams become thinner but are constrained against shape change along their length. This interpretation of the influence of stress-state is supported by the observation that short beams, for which the stress state is closer to biaxial, are more prone to rupture (look ahead to Fig. 7a). In this

regard, short freestanding structures (with a significant biaxial stress) are similar to films-on-substrates. However, the morphology evolution is still quite different. Our hypothesis is that the larger stress in the axial direction promotes void growth along a highly localized "line" perpendicular to the axial direction. This relieves stress in the axial direction and changes the evolution of porosity along the rest of the beam. This suggested mechanism is based on SEM observations of microcracks that occasionally occur in clamped beams (look ahead to Fig. 7c). For films on substrates, the stress is purely biaxial, and localization of defects along a dominant orientation is not as obvious as it is in freestanding structures.

For higher annealing temperatures (i.e. 300 and 400 °C), cantilever porosity decreases considerably as the beam lig-

---

[1] Recall that these cantilevers are those created by beam failure during dealloying, *prior to heat treatment*.
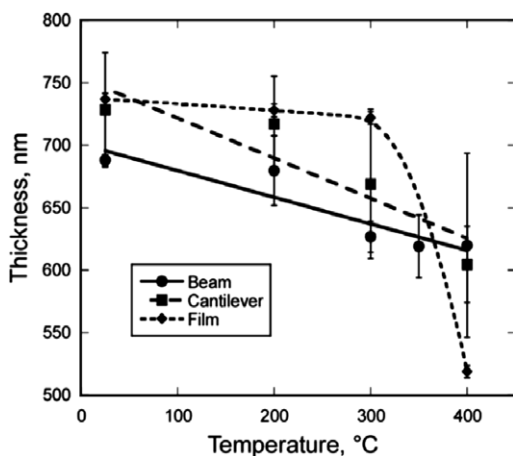
Fig. 4. Thickness for np-Au beams, cantilevers and films as a function of heat-treatment at 200, 300, and 400 °C. Curves are included simply as visual guides.

aments coalesce; this is apparent in Figs. 2 and 3. Measurements of np-Au film thickness with white light interferometry had minimal scatter, while the measurement of beam and cantilever thicknesses via cross-sectional SEM produced larger scatter, as indicated by the error bars in Fig. 4. Fig. 4 shows the measured thickness of the clamped beams and the films on substrates. Beam and cantilever thicknesses decrease rather steadily as a function of annealing temperature, as shown in Fig. 4.

Films on substrates exhibit the greatest morphological changes as a function of annealing temperature, due to different constraints imposed on shape evolution. The substrate prevents planar contraction, and as a result, annealing produces significant changes in film thickness and average pore size. At 300 °C, clearly distinguishable solid Au clusters form and the pore size increases dramatically. The abrupt decrease in thickness between 300 and 400 °C is not currently understood. While it is true that the fully dense Au clusters are slightly larger (while the average pore size is slightly smaller) at 400 °C, this slight

change in porosity is somewhat inconsistent with the dramatic change in thickness. It is speculated that this inconsistency is a consequence of the anisotropic collapse of pores, which are not observable via surface images. That is, at elevated temperatures, the transition from a porous network to "islands" involves fundamental changes in morphology evolution that is accommodated by thermally activated mechanisms, such as surface migration, creep and interdiffusion.

4.2. Mechanical properties of freestanding clamped beams

Typical load–deflection relationships obtained from the nanomechanical characterization approach (described in Section 3.2) are shown in Fig. 5a for clamped beams. Error bars display the standard deviation of nine measurements for each annealing temperature. Only loading curves are shown; unloading curves are virtually identical but have been removed to simplify the figure. The results clearly demonstrate that the fabrication and measurement approaches produce highly repeatable results; Fig. 5a shows the averages from multiple load–deflection cycles on multiple beams. Fig. 5b shows typical stiffness measurements on FIB-cut cantilevers, i.e. the slope of the measured load–displacement relationship obtained at several probe locations. Error bars show the standard deviation of measurements from three distinct FIB-cut cantilevers for each probe location.

The beams are macroscopically brittle, such that the load–deflection relationship is dominated by elastic deformation until fracture; no evidence of macroscopic plastic deformation was observed for any of the tests described here. However, it was observed that np-Au ligaments neck upon tensile fracture (look ahead to Fig. 7d), indicating ligament ductility consistent with the ductile nature of Au. Here, a clear distinction must be made between macroscopic behavior (i.e. over a volume large compared to the void size) and ligament behavior. Macroscopically, the beams are brittle because relatively few ligament failures
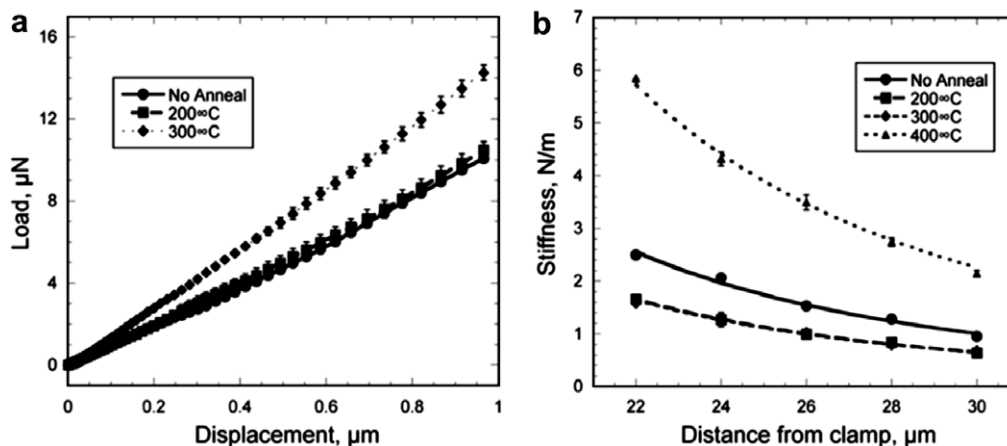

Fig. 5. Typical load–deflection curves for 100 μm-long clamped beams with various heat-treatments (a). Curves are plotted as visual guides. Stiffness of cantilevers created by cutting clamped beams with a FIB, for various heat-treatments; curves are least-squares fit of the form $k = c/l^3$ (b).

can produce a dominant crack, which leads to failure prior to widespread plastic stretching of the ligaments. This observation is consistent with observations made by other groups [12,13].

Indenter penetration into the film itself (as opposed to beam deflection) is also negligible (look ahead to Fig. 7f), as evidenced by the lack of a significant non-linear behavior in the load–deflection relationship. (Contact penetration into the beam itself leads to non-linear behavior because of the growing contact area during penetration.) The relatively blunt Berkovich indenter tip geometry quickly generates a contact stiffness that exceeds the stiffness of the beam; hence, the more compliant mode of beam deflection dominates the response for probe displacements greater than ∼20 nm, as shown in Fig. 5a.

The results shown in Fig. 5a are used to calculate the residual stress in clamped beams. Those of Fig. 5b are used to infer the modulus of the beams using the Euler–Bernoulli beam theory: i.e. $k = Ebh^3/4l^3$, where k is the measured cantilever stiffness, b is the beam width, h is the beam thickness and l is the distance from the clamp to the contact point. Fig. 5b clearly illustrates the predicted relationship between stiffness and probe location, again indicating the lack of any significant plastic deformation or indenter penetration.

The elastic modulus calculated from the stiffness measurements on the FIB-cut cantilevers is shown in Fig. 6, along with error bars that reflect the standard deviation of the modulus that was calculated from data illustrated in Fig. 5a. Note that this modulus corresponds to that of the clamped beams, since the cantilevers were created by cutting intact clamped beams after annealing. (This is a departure from the previous section, where "cantilever" referred to broken beams that were annealed as cantilevers.) The elastic modulus represents the average of multiple values determined from independent stiffness measurements, each of which was an average of multiple load–deflection measurements.

The slight initial decrease of elastic modulus with increasing annealing temperature suggests that there are two competing mechanisms that alter the stiffness of clamped structures, and hence the inferred effective modulus. For larger annealing temperatures, densification dominates the response and the inferred modulus increases, as expected. However, for lower annealing temperatures, tensile stresses crack ligaments (see Fig. 7c) and reduce the effective modulus of the beams. It is speculated that the latter mechanism is more prevalent at lower temperatures, due to decreased mobility of gold atoms; in such scenarios, there is not sufficient time to prevent ligament failure via mass transport (i.e. densification).

The residual stress in the clamped beams was calculated from the stiffness measurements, i.e. the slope of the load–deflection curves. The connection between measured beam stiffness and the residual stress (or pre-tension) requires a brief discussion of the underlying mechanics. The load–deflection response of a pre-tensioned beam subjected to a point load can be determined following the mechanics framework outlined in Refs. [24,25], which accounts for both bending and stretching of the centerline of the beam. The stretching arises from residual stress and/or moderate rotations generated by large deflections.

Perhaps surprisingly, a single analysis produces a solution that captures a wide range of scenarios including: (i) residually stressed membranes (linear behavior arising from significant stretch when bending is negligible); (ii) conventional beam theory for both small and large deflections (i.e. cases where bending dominates and residual stress is negligible); and (iii) non-linear large-deflection response, which culminates in classical non-linear membrane behavior (i.e. cases where stretching dominates and residual stress is negligible). In the present experiments, beam failure generally occurs prior to large deflections, which are generally defined as those of the same order as the beam thickness. As such, the load–deflection curves are essentially linear (see Fig. 5a), with a small degree of
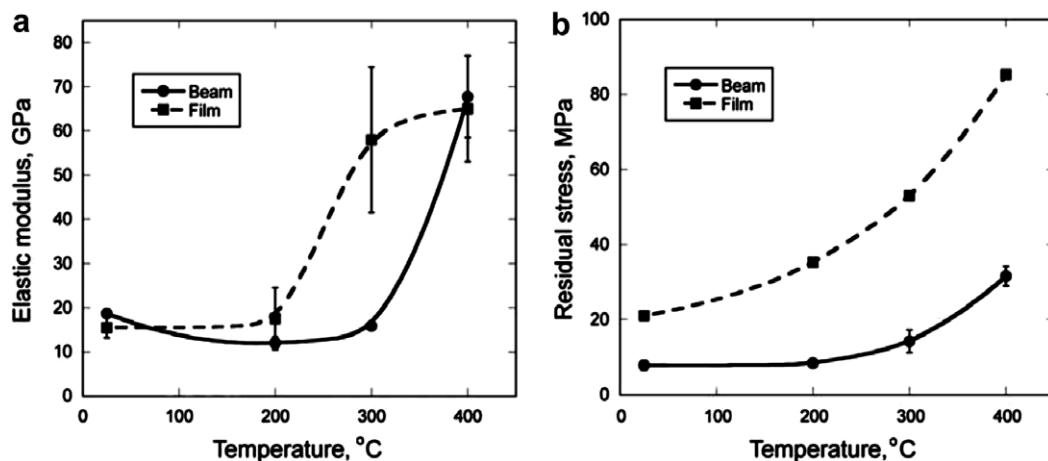

Fig. 6. Elastic modulus of beams extracted from FIB-cut cantilevers at various heat-treatments (a). Residual stress in heat-treated beams calculated from nanoindentation data and residual stress in films extracted from wafer curvature experiments (b). Curves on both figures are visual guides.
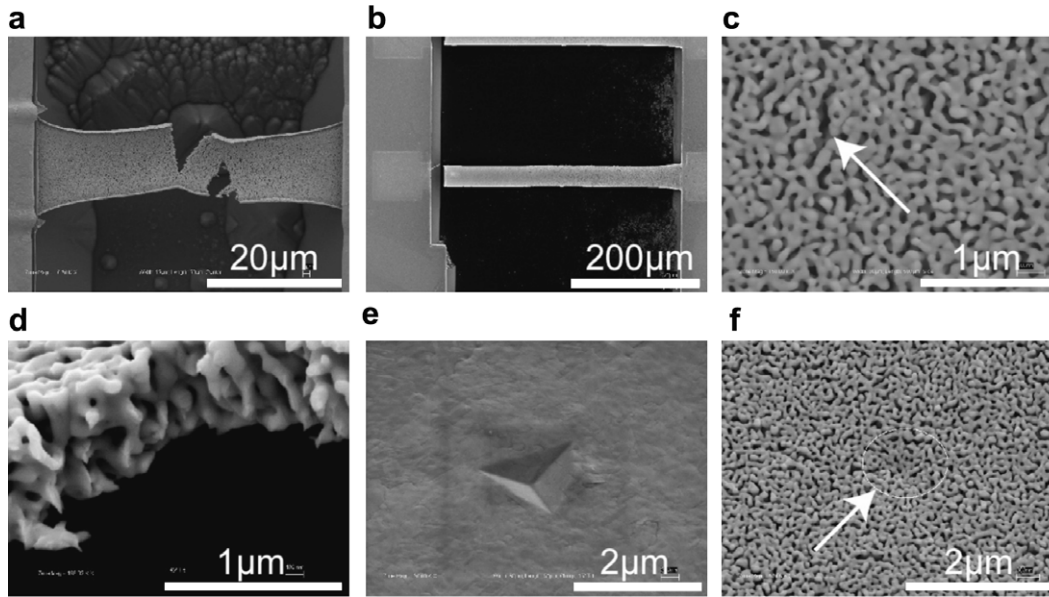
Fig. 7. A np-Au beam experiencing tensile fracture during heat-treatment at 400 °C (a). Tensile beam failure at beam-clamp interface due to skipping necessary heat-treatment prior to dealloying (b). Micro-crack formation during heat-treatment at 200 °C (c). Micro-necking at the location where np-Au beam was broken due to surface damage by a tweezer (d). Nanoindenter tip mark on electroplated Au clamp (e), and np-Au beam surface (f).

non-linearity that arises when the deflection becomes comparable to the film thickness. In the following, the residual stress is extracted from the stiffness of the linear portion of the load–deflection measurement, which for nearly all cases spans the entire range of the measurement.

For very small loads, the initial load–deflection response is linear, regardless of whether or not bending or residual stress dominates. The initial stiffness for the structure – at zero load – is given by [25]:

$$\hat{k} \equiv \frac{k}{k_0} = \frac{\left(\frac{\varepsilon_0}{\bar{h}^2}\right)^{3/2}}{\sqrt{\frac{\varepsilon_0}{\bar{h}^2}} - \frac{\tanh\sqrt{\frac{3\varepsilon_0}{\bar{h}^2}}}{\sqrt{3}}} \tag{1}$$

where $k_0 = 2Eb\bar{h}^3/L^3$ is the stiffness of the beam without pre-stretch (where L is the beam length and $\bar{h} = h/L$), and $\varepsilon_0 = \sigma_0/E$ is the residual strain arising from the residual stress, σ_0. One may expand this for small values of $\varepsilon_0/\bar{h}^2$ to obtain the simplified result:

$$\hat{k} = 1 + \frac{6\varepsilon_0}{5\bar{h}^2} = 1 + \frac{6\sigma_0 L^2}{5E\bar{h}^2}. \tag{2}$$

This approximation is excellent over a very broad range, with less than 10% error for $\varepsilon_0 < 10\bar{h}^2$. It is worth noting that the scaling implies that the stiffness is a strong function of residual stress for beams with large aspect ratios. For example, a residual strain of $\varepsilon_0 = 1 \times 10^{-4}$ more than doubles the measured stiffness of a beam with $L > 100h$, as is the case here.

The residual stress in the beams that was calculated using Eq. (2) is shown in Fig. 6b. Error bars are due to the standard deviation from nine distinct load–displacement measurements per annealing temperature. The measured film thickness (shown in Fig. 4) was used in the

calculation. The tensile residual stress increased monotonically with increasing annealing temperature for np-Au beams, as one might expect from the observations of porosity evolution discussed earlier. As pores coalesce, the np-Au densifies, and the accompanying longitudinal strain translates into increasing tensile stress with heat-treatment. Residual stress increased from ∼7 to ∼32 MPa over the range of annealing temperatures. In light of the discussion regarding ligament cracking (as a mechanism to reduce the inferred effective modulus), it is apparent that densification dominates the response at higher annealing temperatures. Although the residual stress increases continually with annealing temperature, the likelihood of ligament fracture decreased due to the growth of ligament size (as evidenced by decreasing porosity).

4.3. Mechanical properties of blanket films

The elastic modulus of the films on substrates determined via nanoindentation is shown in Fig. 6a. The error bars display the standard deviation of 10 indentations on each sample annealed at a different temperature. The dramatic increase in densification arising from pore coalescence at elevated temperatures is clearly evident; one obtains results that are within 70–90% of the modulus of bulk gold samples. (Note that the modulus of the AuAg alloy is nearly identical to that of gold since Au and Ag have very similar moduli, e.g. nanoindentation of fully dense AuAg films on substrates yields 78 ± 4 GPa.) This is entirely consistent with the porosity changes described earlier (e.g. the percent porosity displayed in Fig. 3).

Wafer curvature measurements were performed to study the residual stress in np-Au films following heat-treatment.

A scanning laser wafer curvature apparatus was used to measure the radius of curvature of the wafers, and the residual stress was calculated using a modifed form of Stoney's formula [24]:

$$\sigma_0 = \frac{K_{stress}(h_{Si})^2}{\rho \cdot h_{film}} \tag{3}$$

where σ_0 is the residual stress in MPa, K_{stress} is the stress constant for a (100)Si wafer accounting for the elastic modulus and the Poisson's ratio of the substrate, h_{Si} is the thickness of the Si wafer, ρ is the radius of curvature and h_{film} is the film thickness.

The effect of the intrinsic curvature of each wafer was automatically removed from the measurements by the software provided with the wafer curvature apparatus. In order to calculate the residual stress for the np-Au film, the radius of curvature due to the adhesion layer was subtracted from the measured radius of curvature for the Cr/Au/np-Au multilayer. The results are plotted in Fig. 6b. The wafer curvature measurements produce minimal scatter and hence error bars are not visible. A more pronounced increase in stress for the np-Au films was observed (as compared to the beams), which was consistent with its pronounced pore coalescence and the biaxial constraint inherent to the film-on-substrate geometry. The net stress change was from 21 to 85 MPa through the annealing cycle. Finally, the relaxation of stress in np-Au films over 1 day at room temperature was negligible. Dealloying of Cr/Au-coated control wafers did not result in a measurable change in stress of the adhesion layer.

It is worth noting that when AuAg on Cr/Au was dealloyed to produce the np-Au films, the residual stress decreased from 125 to 21 MPa. Clearly, dealloying will reduce the biaxial tensile stress in the as-deposited alloy film through morphological change. The stress in the dealloyed films is approximately twice that in the dealloyed beams; this is probably a consequence of the difference in geometric constraint. Interestingly, heat treatment before dealloying blanket films has relatively little effect on the final stress state, in contrast to freestanding structures (as will be elucidated in Ref. [20]).

4.4. Observations of microstructure damage

Several different deformation and fracture modes were observed on the structures during the experiments; Fig. 7 provides a survey of some of these incidents. Very short beams (in comparison to the width) are more prone to rupture during dealloying (Fig. 7a); this is presumably due to the fact that the stresses perpendicular to the principle axis of the beam will be higher. Put another way, short beams have higher components of biaxial stress that promote rupture. The longer beams used for generating the results described earlier do not exhibit such failure modes – presumably the stress-state is closer to uniaxial and therefore lower.

For a small number of beams, intrinsic defects introduced by the fabrication process lead to beam rupture during dealloying; this typically occurs at the clamped edges, as shown in Fig. 7b. As mentioned earlier, this failure mode is virtually eliminated by heat-treatment prior to dealloying [18]. Fig. 7c illustrates evidence of ligament failure (i.e. microcracking) in clamped beams during annealing, presumably driven by tensile stresses arising during pore evolution. These microcracks appeared in clamped beams for heat-treatments at 200 °C, but were not observed for higher temperatures (or other geometries).

Occasionally, failure was simply caused by handling (i.e. accidentally breaking a beam when handling the sample with tweezers); this afforded the opportunity to observe the porosity in the thickness direction, as shown in Fig. 7d. Such observations support the conclusion that the porosity is broadly isotropic, such that the observed surface porosity is a meaningful measure of morphology. Finally, Fig. 7e and f illustrate the permanent deformation resulting from indentation; the surface-finding step of the nanoindentation procedure left a visible mark on the electroplated Au clamp (Fig. 7e), but left negligible impressions on freestanding beams (Fig. 7f).

5. Concluding remarks

Freestanding np-Au structures and np-Au films on substrates were subjected to different annealing temperature to explore the effects of porosity/morphology evolution on mechanical properties. Despite the common coarsening effect of heat on porosity, each type of np-Au sample with a different geometric constraint exhibits different types of porosity evolution. The average pore size for cantilevers and clamped beams decreased for all annealing temperatures; for 200 °C, there was evidence of ligament failure, which reduced the effective modulus inferred from beam deflection experiments. Films, on the other hand, generally displayed rapidly increasing average pore size. Residual stress in both the beams and films increased with increasing annealing temperature, due to the densification of np-Au. This fundamental thermomechanical study of np-Au should offer insight regarding more effective microfabrication processes and use of np-Au in sensors and actuators. Ongoing work is investigating the effects of heat-treatment on freestanding AuAg beams and AuAg films to more exhaustively quantify the effect of annealing prior to dealloying [20].

References

[1] Huang J-F, Sun I-W. Adv Funct Mater 2005;15:989.
[2] Lavrik NV, Tipple CA, Sepaniak MJ, Datskos PG. Biomed Dev 2001;3:35.

[3] Erlebacher J, Aziz MJ, Larma A, Dimitrov N, Sieradzki K. Nature 2001;410:450.

[4] Erlebacher J. J Electrochem Soc 2004;151:C614.

[5] Ding Y, Kim Y, Erlebacher J. Adv Mater 2004;16:1897.

[6] Senior NA, Newman RC. Nanotech 2006;17:2311.

[7] Kelly RG, Young AJ, Newman RC. The characterization of the coarsening of dealloyed layers by EIS and its correlation to stress-corrosion cracking. In: Scully JR, Silverman D, editors. Electrochemical impedance: analysis and interpretation. West Conshohocken, PA: ASTMaterials; 1993. p. 94.

[8] Kelly RG, Frost AJ, Shahrabi T, Newman RC. Metall Trans 1991;22A:531.

[9] Sieradzki K, Corderman RR, Shukla K. Philos Mag A 1989;59:713.

[10] Dursun A, Pugh DV, Corcoran SG. J Electrochem Soc 2003;150:B355.

[11] Li R, Sieradzki K. Phys Rev Lett 1992;68:1168.

[12] Biener J, Hodge AM, Hamza AV. Appl Phys Lett 2005;87:121908.

[13] Biener J, Hodge AM, Hamza AV, Hsiung LM, Satcher JH. Appl Phys Lett 2005;97:024301.

[14] Volkert CA, Lilleodden ET, Kramer D, Weissmüller J. Appl Phys Lett 2006;89:061920.

[15] Hieda M, Garcia R, Dixon M, Daniel T, Allara D, Chan MHW. Appl Phys Lett 2004;84:628.

[16] Ji C, Searson PC. Appl Phys Lett 2002;81:4437.

[17] Liu Z, Searson PC. J Phys Chem B 2006;110:4318.

[18] Zhu J, Seker E, Bart-Smith H, Begley MR, Reed M, Kelly R, et al. Appl Phys Lett 2006;89:133104.

[19] Parida S, Kramer D, Volkert CA, Rösner H, Erlebacher J, Weissmüller J. Phys Rev Lett 2006;97:035504.

[20] Seker E, Gaskins TJ, Bart-Smith H, Begley MR, Zhu J, Reed M, et al. Acta Mater; submitted for publication.

[21] WCIF ImageJ 1.37a, National Institutes of Health, USA. <http://rsb.info.nih.gov/ij/>.

[22] Sezgin M, Sankur B. J Electron Imaging 2004;13:146.

[23] Maner KC, Begley MR, Oliver WC. Acta Mater 2004;52:5451.

[24] Freund LB, Suresh S. Thin film materials. Cambridge: Cambridge University Press; 2003.

[25] Begley MR, Barker NS. J Micromech Microeng 2006;17:350.